Bioactive Materials 16 (2022) 334–345

Contents lists available at ScienceDirect

Bioactive Materials

journal homepage: www.keaipublishing.com/en/journals/bioactive-materials

Next-generation finely controlled graded porous antibacterial bioceramics for high-efficiency vascularization in orbital reconstruction

Jingyi Wang [a], Yiyu Peng [a], Menglu Chen [a], Xizhe Dai [b], Lixia Lou [a], Changjun Wang [a], Zhaonan Bao [c], Xianyan Yang [c], Zhongru Gou [c,**], Juan Ye [a,*]

[a] Eye Center, The Second Affiliated Hospital, Zhejiang University School of Medicine, Zhejiang Provincial Key Lab of Ophthalmology, Hangzhou, 310009, PR China
[b] Department of Ophthalmology, The Children's Hospital, Zhejiang University School of Medicine, National Clinical Research Center for Child Health, Hangzhou, 310051, PR China
[c] Zhejiang-California International NanoSystems Institute, Zhejiang University, Hangzhou, 310029, PR China

ARTICLE INFO

Keywords:
Graded porous scaffolds
Fibro-vascularization
Antibacterial
Hardystonite
Orbital implants

ABSTRACT

Eyeball loss due to severe ocular trauma, intraocular malignancy or infection often requires surgical treatment called orbital implant reconstruction to rehabilitate the orbital volume and restore the aesthetic appearance. However, it remains a challenge to minimize the postoperative exposure and infection complications due to the inert nature of conventional orbital implants. Herein, we developed a novel Ca–Zn-silicate bioceramic implant with multi-functions to achieve the expected outcomes. The porous hardystonite ($Ca_2ZnSi_2O_7$) scaffolds with triply periodic minimal surfaces (TPMS)-based pore architecture and graded pore size distribution from center to periphery (from 500 to 800 μm or vice versa) were fabricated through the digital light processing (DLP) technique, and the scaffolds with homogeneous pores (500 or 800 μm) were fabricated as control. The graded porous scaffolds exhibited a controlled bio-dissolving behavior and intermediate mechanical strength in comparison with the homogeneous counterparts, although all of porous implants presented significant antibacterial potential against *S. aureus* and *E. coli*. Meanwhile, the pore size-increasing scaffolds indicated more substantial cell adhesion, cell viability and angiogenesis-related gene expression *in vitro*. Furthermore, the gradually increasing pore feature exhibited a stronger blood vessel infiltrating potential in the dorsal muscle embedding model, and the spherical implants with such pore structure could achieve complete vascularization within 4 weeks in the eyeball enucleation rabbit models. Overall, our results suggested that the novel antibacterial hardystonite bioceramic with graded pore design has excellent potential as a next-generation orbital implant, and the pore topological features offer an opportunity for the improvement of biological performances in orbital reconstruction.

1. Introduction

Eyeball removal by evisceration or enucleation is typically performed as a treatment for severe ocular trauma, uncontrolled intraocular infection, and life-threatening intraocular malignancies [1]. After removing the eye, inserting an orbital implant into the anophthalmic socket is an optional way to rehabilitate orbital volume and restore the acceptable aesthetic appearance of patients. In recent years, porous implants have attracted more attention because they are beneficial for allowing fibrovascular ingrowth and better integration with the host tissue. Such revascularization can reduce the incidence of complications such as migration, exposure and secondary infection [2,3]. Among the clinically available porous orbital implants, Medpor and hydroxyapatite (HA) implants are respectively the representatives of organic and inorganic material products due to their good biocompatibility [3]. However, they still have a number of formidable limitations such as delayed vascularization, uncontrolled surface microstructures or difficulties in pore size/interconnection adjustment [4–6]. Considering the existing drawbacks of current orbital implants and their treatment outcomes, the means to develop a novel multifunctional orbital implant to improve the

Peer review under responsibility of KeAi Communications Co., Ltd.
* Corresponding author. Eye Center, The Second Affiliated Hospital, Zhejiang University School of Medicine, Zhejiang Provincial Key Lab of Ophthalmology No.88 Jiefang Rd, Hangzhou, 310009, China.
** Corresponding author. Zhejiang-California International NanoSystems Institute Zhejiang University, Yuhangtang Road 866, Hangzhou, 310058, China.
E-mail addresses: zhrgou@zju.edu.cn (Z. Gou), yejuan@zju.edu.cn (J. Ye).

https://doi.org/10.1016/j.bioactmat.2021.12.028
Received 17 September 2021; Received in revised form 25 December 2021; Accepted 26 December 2021
Available online 2 January 2022

integration rate without side effects has become an outstanding research question.

An ideal orbital implant should exhibit excellent biocompatibility and a defined porous structure for vascularization, very limited degradation for long-term *in situ* mouldability, good antibacterial properties to inhibit bacterial growth and secondary infections, as well as adequate mechanical resistance for surgical insertion [7]. Some multifunctional bioactive ceramics have shown great potential in the development of new-generation orbital implants through their intrinsic angiogenic and antibacterial effects associated with the release of bioactive inorganic ions [8,9]. Hardystonite ($Ca_2ZnSi_2O_7$) has been studied as a recognized biocompatible bioceramic in a variety of biomedical fields [10–12]. This bioceramic may enhance the proliferation, differentiation of osteogenic cell and promote the expression of osteoblast-related genes [13,14]. Previous study has indicated that hardystonite-coated Ti substrates exhibit remarkable chemical stability and considerable antibacterial potential [15,16]. In the field of wound management, it was found that the synergistic effect of Zn and Si ions from hardystonite can readily inhibit bacterial growth, promote endothelial cell proliferation, and stimulate angiogenesis and wound healing [17,18]. Moreover, this bioceramic exhibits good sintering and mechanical properties, which are beneficial for 3D printing high-porosity constructs with appropriate structural stability [19]. Therefore, hardystonite bioceramic is an outstanding candidate for the development of durable orbital implants for orbital reconstruction.

On the other hand, the introduction of porous architectures to biomaterials has broadened their application in tissue engineering. The interconnected pore structure allows cell migration and the exchange of nutrients, as well as neo-vascularization prior to tissue formation [20]. The pore characteristics of porous scaffolds including pore geometry, pore size, connectivity, and porosity, which have been proved as highly influential in altering the behaviors (mechanical, physicochemical, biological) of the biomaterials [21–23]. It has been reported that large pore size is favorable for vascularization, and a pore size greater than 300 μm was recommended for capillaries growth [24]. However, larger pore size or highly porosity often leads to lower mechanical strength, faster degradation and structural instability. Therefore, the graded pore design may be an alternative to compromise between the limitations of porous structure and biological performances. Li et al. reported that the graded pore architecture exhibits a heterogeneous vascularization behavior especially the larger pores at the periphery may improve angiogenesis and osteogenesis [25]. However, the fabrication of a fully interconnected graded porous structure by conventional methods is complicated, which procedures including template leaching, graded particle sintering, solid free form fabrication, freeze-drying, and so on [26–28]. In contrast, the digital light processing (DLP)-based 3D printing technique has made it easier and more convenient to fabricate complex graded porous constructs. The computer-assisted design (CAD) can be simultaneously used to precisely control the pore geometry and interconnectivity of porous scaffolds [29]. Recently, triply periodic minimal surfaces (TPMS)-based pore architectures including pore unit cells, such as diamond, gyroid, primitive and IWP, have been widely utilized in tissue engineering due to their mathematically controllable pore size, interconnected porosity, huge surface area and superior mechanical support [30]. Studies targeted the 3D printing of porous metallic scaffolds with TPMS-based pore architecture for bone tissue regeneration, which structures may easily mimic the natural trabecular bone structure of human bones [31,32]. However, the application of this topological design of DLP-based graded porous bioceramic implant has not yet been reported for orbital reconstruction.

Based on the above concerns, we aimed to develop the novel multifunctional porous hardystonite bioceramics with graded pore architectures as a next-generation orbital implant. The roles of graded pore design in the structural stability and biological performances were systematically evaluated *in vitro* and *in vivo*. In particular, the hardystonite scaffolds with graded pore size distribution from center to periphery (from 500 to 800 μm or vice versa) were printed by the DLP technique. The IWP unit cell this paper used for topological design were firstly fabricated by Abueidda et al. [30]. and has been proven to be successfully utilized in preparing bioceramic scaffolds with completely interconnected and accurately controlled pore structure in our previous study [33]. To our knowledge, the present work is the first to investigate a single-phase multifunctional bioceramic implant with precisely tailored graded pore architecture to accelerate orbital reconstruction *in situ*.

2. Materials and methods

2.1. Materials

The reagent-grade calcium nitrate tetrahydrate ($Ca(NO_3)_2{\cdot}4H_2O$), zinc nitrate hexahydrate ($Zn(NO_3)_2{\cdot}6H_2O$), nitric acid (HNO_3), and tetraethyl orthosilicate ($(C_2H_5O)_4Si$, TEOS) were purchased from Sinopharm Reagent Co., Ltd., without further purification. The organic reagents used for the preparation of printing resin included 1,6-hexanediol diacrylate (HDDA, Alfa Aesar Co. Ltd.), ethoxylated pentaerythritol tetraacrylate (PPTTA, DSM-AGI Co. Ltd.), and 2,4,6-trimethyl-benzoyl-diphenylphosphine oxide (TPO, BASF (China) Co., Ltd.). Trishydroxymethylaminomethane (Tris) was applied to prepare the Tris buffer (0.05 M, pH ~7.40). The porous HA scaffolds and the synthetic HA orbital implants (Ø 12 mm), which have an open and interconnected porous structure (with porosity ~65%), were obtained from Puchuan Biomaterial Co., China.

2.2. Synthesis of ceramic powders

The hardystonite powders were synthesized by the previously described sol-gel process [34]. Briefly, the TEOS was mixed with water and HNO_3, and hydrolyzed while stirring for 30 min. Then, $Ca(NO_3)_2{\cdot}4H_2O$ and $Zn(NO_3)_2{\cdot}6H_2O$ were added to the mixture in a stoichiometric ratio. After stirring for 5 h at room temperature, the solution was aged at 60 °C for 24 h and dried at 120 °C for 48 h to obtain the dry gel. Following calcination at 1250 °C for 3 h in a muffle furnace, the powders were ground in a planetary ball mill for 6 h to reach particle sizes below 5 μm. The crystallization of the powder was identified by X-ray diffraction (XRD; Rigaku Co., Japan).

2.3. Manufacture of bioceramic scaffolds through DLP

Four groups of scaffold models with different pore size distribution were designed based on 1.5-mm IWP unit cell using the Materialise Magics 21.0 software (Fig. 1A). The graded porous scaffolds with radially changing pore size from center to perimeter were composed of three layers (see Fig. 1B&C). Specifically, four groups of scaffold models (Ø 9 × 5 mm) were fabricated, including a uniform pore structure with 500 μm in pore size (P500), a graded pore structure with pore size gradually changing from 800 to 500 μm from center to periphery (P800-500), a graded pore structure with pore size gradually changing from 500 to 800 μm from center to periphery (P500-800), and a uniform pore structure with 800 μm in pore size (P800) (Fig. 1D). The 3D models of spherical implants (Ø 12 mm) with two different graded pore structures (sP800-500, sP500-800) were designed for the *in situ* animal model of enucleation.

All 3D porous models were sliced to printing files and imported into the ceramic DLP 3D printer (Ten Dimensions Technology Co., China). The printing process was based on the photopolymerization of a mixture of resin and hardystonite powders (see Fig. 1E). The resin was composed of mHDDA and mPPTTA as monomers with a mass ratio (mHDDA: mPPTTA) of 7:1, and TPO as the photo-initiator. The resin and ceramic powders were mixed in a mass ratio of 2:3. After mixing in a ball mill for 1 h, the slurry was poured into the slurry tank. The light intensity was 10,000 $\mu W/cm^2$, accompanied by an exposure time of 2–3 s for each

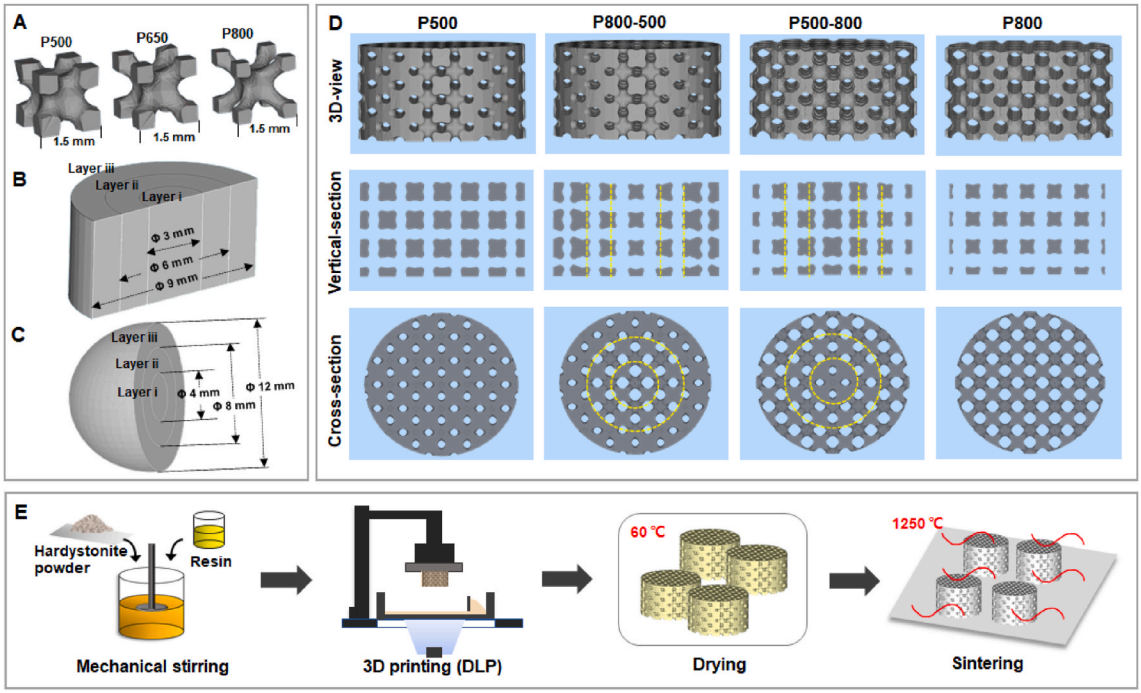

Fig. 1. (A) Pore unit cells (IWP) with gradually increased pore size. Three layers (Layer i, ii and iii) of graded pore distribution in (B) a cylindrical sample and (C) a spherical sample. (D) The CAD models of four different porous structure design. Yellow dotted lines show the boundaries between different layers in a graded porous scaffold. (E) Scheme illustration of the preparation process for digital light processing 3D printed porous bioceramic scaffolds.

layer. Under these conditions, the slurry was solidified with a definite accuracy and thickness, and stacked into the ideal 3D structure.

After completing the printing process, the samples were ultrasonically washed in deionized water to remove any residual slurry and dried at 60 °C overnight. Subsequently, the porous green bodies were sintered in a micro-controller-regulated temperature furnace (Kejing Co., Hefei, Anhui, China) at a target temperature of 1250 °C with a heating rate of 2 °C/min, held at the target temperature for 3 h, and then left to cool naturally. The sintered scaffolds were also analyzed by XRD.

2.4. Morphology and structural analysis

The outward morphology and pore architectures of the porous samples before and after sintering were observed using a digital camera (iPhone X, Apple). The linear shrinkage of the cylindrical samples was calculated by measuring the height and diameter using a sliding caliper before and after sintering. The surface roughness of the samples was investigated by a non-contact optical profiler (WykoNT9100, Veeco, America). Each sample was measured five times at randomly selected locations (300 × 200 μm). The parameter (Roughness average, Ra) acquisition and image processing were performed using built-in software (Vision 4.2). High-resolution micro-computed tomography (micro-CT, vivaCT100, Scanco Medical, Zurich, Switzerland) was performed for structural characterization. A tube current of 80 μA, a tube voltage of 80 kV, a scan time of 8 min, and a resolution of 14 μm were applied during the scanning process. The 3D reconstructed images and 2D section images were generated using built-in device software (IAW, Siemens, Germany). The region of sample was selected as the region of interest (ROI). The total ROI volume, scaffold volume, scaffold surface area to scaffold volume ratio (SVR), average strut spacing (pore size) and total porosity (defined as: *Porosity* = (1- scaffold volume/ROI volume) × 100%) were subsequently calculated. In addition, the top-view surface and fracture surface of porous scaffolds were analyzed by scanning electron microscopy (SEM; GEMINI 300, ZEISS, Germany).

2.5. Mechanical characterization

The compressive resistance of the porous scaffolds (Ø 9 × 9 mm^3; n = 3) was tested using a universal testing machine (Instron 5566) with a 10-kN load cell at a crosshead speed of 5 mm/min.

2.6. In vitro degradation test

In order to evaluate the degradation behavior (bio-dissolution *in vitro*), four groups of weighed scaffolds (m_0, Ø 9 × 5 mm^3; $n = 3$) were immersed in Tris buffer with an initial pH of 7.4 in a thermostatic water-bath at 37 °C with a scaffold/buffer ratio of 1.0 g/50 mL. At each time point, the supernatant (0.5 mL) was collected for ion concentration analysis (ICP-OES; Thermo, UK) and refresh Tris buffer (0.5 mL) was added. After immersion for 1–6 weeks, the samples were rinsed with absolute ethanol, dried at 60 °C for 12 h, and finally weighed (m_t). The mass residue was calculated using the following formula: mass residue (%) = $m_t/m_0 \times 100\%$.

2.7. In vitro antibacterial assay

The antibacterial activity of the porous bioceramic scaffolds was evaluated with *Staphylococcus aureus* (*S. aureus*, ATCC 25923) and *Escherichia coli* (*E. coli*, ATCC 8099). The bacteria were suspended and diluted to 5.0 × 10^7 CFU/mL using sterilized water. The porous HA scaffolds and four groups of hardystonite scaffolds were placed in the tissue culture plate, followed by the inoculation of 10 μL of bacterial suspension onto each scaffold. The well without scaffolds was used as control. The scaffolds were incubated at 37 °C under ≥90% relative humidity for 12 h. At this time point, 1 mL of PBS was added to each well to suspend the remaining bacteria, and 100 μL of the suspension was inoculated onto the Luria–Bertani agar plate. The plates were then incubated at 37 °C for 24 h, and the number of colony-forming units (CFU) was counted. The results were expressed as:

Antibacterial ratio (%) = (CFU count of control – CFU count on scaffolds)/CFU count of control × 100%.

2.8. Cell culture in vitro

Human umbilical vein endothelial cells (HUVECs) were obtained from the Cell Culture Center, Chinese Academy of Medical Science (Shanghai, China). These cells were cultured in the endothelial cell medium (ECM, Science Cell) in an incubator at 37 °C with 5% CO_2. All scaffolds were sterilized with 75% ethanol prior to washing in PBS.

2.8.1. Fluorescence analysis

In order to assess the cell adhesion behavior, four groups of hardystonite scaffolds were placed into 24-well tissue culture plates and immersed in ECM for 2 h. Next, 1×10^4 cells were seeded onto the scaffolds and cultured for 12 h, then the samples were washed in PBS and fixed with 4% (w/v) paraformaldehyde for 20 min. After rising in PBS, the fixed cells were permeabilized with 0.1% Triton X-100 for 20 min. Then, 5 μg/mL fluorescein isothiocyanate (FITC) -conjugated phalloidin (Invitrogen) was added to label the cell actin, and 10 μg/mL 4′,6-diamidino-2-phenylindole (DAPI) (Invitrogen) was added to separately label the cell nuclei. Finally, the cells were observed under a fluorescence microscope (Leica, Germany). A semiautomatic image analysis system (Image J) was utilized to calculate the fluorescence intensity of FITC and DAPI (n = 4).

2.8.2. Cell viability

In order to evaluate the viability of cells, the Cell Counting Kit-8 (CCK-8, Dojindo, Japan) assay was used. The HUVECs were seeded onto scaffolds at a concentration of 1×10^4 cells/cm^2. The cell culture plates without scaffolds were used as the blank control, and HA scaffolds were used as the positive control. A volume of 0.5 mL α-MEM supplemented with 10% CCK-8 was added into each well at 1, 3 and 5 days. Following incubation at 37 °C for 2 h, 100 μL of the above-mentioned solution was transferred to a 96-well plate, and the absorbance of wells at 450 nm was measured by a microplate reader (Infinite F50; TECAN, Hombrechtikon). Four parallel specimens were used to measure the cell viability in each group.

2.8.3. Quantitative polymerase chain reaction (qPCR) analysis

The expression of two angiogenesis-related genes, the vascular endothelial growth factor (VEGF) and the basic fibroblast growth factor (bFGF), was analyzed by quantitative PCR (qPCR) at 5 days. Total RNA was extracted using a RNA purification kit (EZ Bioscience) following the manufacturer's instructions. The concentration of total RNA was determined using NanoDrop 2000 (Thermo Fisher Scientific Inc., USA). The isolated RNA was reverse-transcribed into complementary DNA (cDNA) using a reverse transcription reagent kit (Takara). The expression of target genes was detected on a PCR system (Bio-Rad, Hercules, CA, USA) following the manufacturer's guidelines. Data were normalized to the β-actin. The applied forward and reverse primer sequences were shown in Table 1.

2.9. Animal model and experimental design

The animal experiment was approved by the Animal Ethics Committee of the Second Affiliated Hospital of Zhejiang University (2018–333). To evaluate the scaffold's biocompatibility and vascularization ability *in vivo*, nine male adult New Zealand rabbits (2.5–3.0 kg) were used in the dorsal muscle embedding experiment. The animals were anesthetized by the intravenous injection of 3% phenobarbital sodium (1 mL/kg) and placed in prone position with the front and hind legs fixed. After sterilization with 5% povidone-iodine, four 2-cm incisions were made longitudinally on the dorsum of the rabbits. Then, the dorsal muscle was blunt dissected to create four intramuscular pockets, and each scaffold was inserted into an intramuscular pocket. In a rabbit, four scaffolds (Ø 9 × 5 mm^3) were implanted, including P500, P800-500, P500-800 and P800. At 2, 4 and 6 weeks, the rabbits were euthanized by an overdose of pentobarbital sodium, and the specimens were harvested and carefully observed.

In addition, six male adult New Zealand rabbits (2.5–3.0 kg) were subjected to enucleation of the right eye for the *in situ* orbital implantation experiment. The synthetic HA orbital implant (Ø 12 mm) was used as control. The animals were randomly divided into three groups (HA, sP800-500 and sP500-800). After inducing anesthesia by the intravenous injection of 3% sodium phenobarbital, the periorbital area of each rabbit was sterilized with 5% povidone-iodine. A 360° conjunctival peritomy was performed adjacent to the corneal limbus. The conjunctiva and Tenon's capsule were separated from the sclera. Four rectus muscles were detached from the globe. After clamping for 5 min, the optic nerve was transected, and the globe was removed. The spherical implant with 12 mm diameter was inserted into the anophthalmic socket, and the four remaining rectus muscle stumps were knotted together end-to-end anterior to the implant. The Tenon's capsule and the conjunctiva were closed in layers. The rabbits were euthanized 4 weeks after implantation and the specimens were carefully harvested from the orbit.

Table 1
Primers for real-time PCR experiments.

Gene	Direction	Primer sequence (5′-3′)
VEGF	Forward	GAGCCTTGCCTTGCTGCTCTA
	Reverse	CACCAGGGTCTCGATTGGAT
bFGF	Forward	AAAAACGGGGGCTTCTTCCT
	Reverse	TGTAGCTTGATGTGAGGGTCG
β-Actin	Forward	CAACGGCTCCGGATGTGC
	Reverse	CTCTTGCTCTGGGCCTCG

2.10. Histological analysis

The harvested samples were fixed immediately in paraformaldehyde solution (4%; pH ~7.2) for histological analysis. After fixing for 2 days, the samples were dehydrated with successive dilutions of alcohol solution from 80 to 100%, and then embedded in polymethylmethacrylate (PMMA). After hardening, the specimens were cut into sections with 100–200 μm thickness through the center by a saw microtone (SP1600, LEICA). Finally, the sections were ground and polished to a final thickness of 40–50 μm, and then stained with H&E.

The stained sections were observed and recorded using light microscopy (DMLA, Leica). A semiautomatic image analysis system (Image J) was employed to calculate the number and the diameter of blood vessels (n = 3) for samples in the dorsal muscle embedding experiment. The fibrovascularization degree of spherical scaffolds was defined as the depth of ingrowth fibrovascular tissue (from the edge of the implant toward the center) divided by the radius of the implant [35].

2.11. Statistical analysis

All numerical data were expressed as mean value ± standard deviation (SD) and analyzed by SPSS 19.0 software (SPSS, Chicago, IL, USA). One-way analysis of variance (ANOVA) was performed for statistical analysis, and the results were considered to be significant when $p < 0.05$.

3. Results

3.1. Morphological and structural characteristics of scaffolds

The outward appearance of (sintered) porous samples was observed by a digital camera (Fig. 2A). It could be seen that all scaffolds retained the defined porous structure before and after sintering without obvious nonlinear shrinkage or deformation. The graded pore structure in P800-500 and P500-800 scaffolds could be clearly seen in the top view of the samples. Meanwhile, the 2D/3D images reconstructed by micro-CT

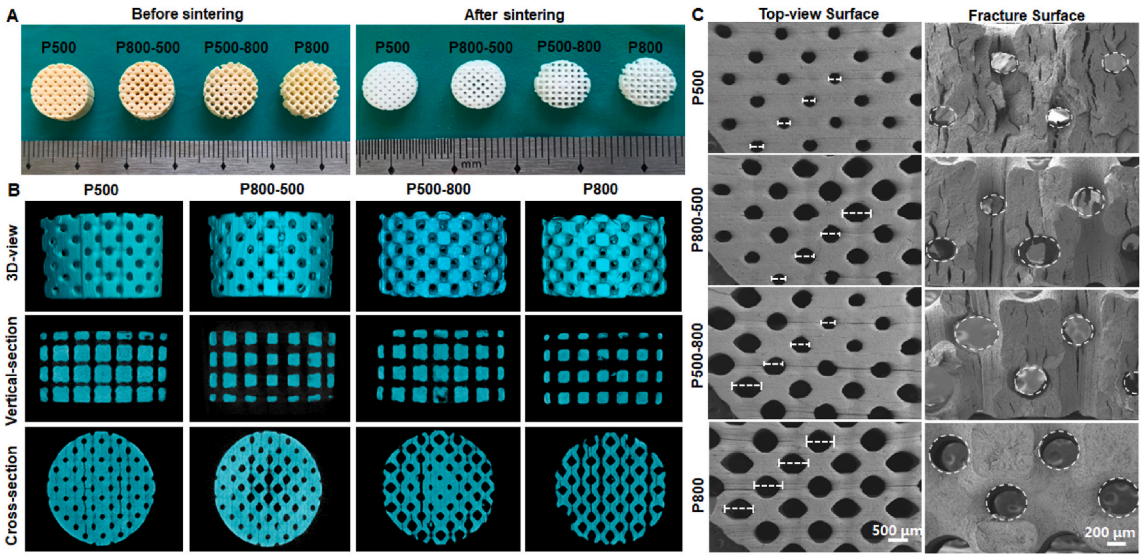

Fig. 2. Primary morphology and structure observation for the hardystonite bioceramic scaffolds with four different pore architectures. (A) Outward appearance before and after sintering. (B) The 3D/2D images reconstructed by micro-CT of the sintered scaffolds. (C) SEM images of the top-view surface and fracture surface morphology of the sintered scaffolds.

confirmed the internal (graded) pore structure of the macroporous bioceramics (Fig. 2B). The strut thickness and pore size were radially graded changing for the P800-500 and P500-800 scaffolds, while the strut thickness and pore size remained uniform for the P500 and P800 scaffolds. The porous architectures were matched well with the designed 3D porous models (see Fig. 1D). The graded pore architectures were also confirmed by SEM observation of the top-view and fracture surface of samples (Fig. 2C). In addition, the XRD analyses (Fig. S1) confirmed the single-phase hardystonite (PDF #27–0088) of the ceramic powders and the porous scaffolds.

The theoretical values of porous structure designed by computer and the actual values measured by micro-CT for the four groups of scaffolds were listed in Table 2. The pore size and porosity of the sintered samples were both slightly reduced in comparison with the theoretical value, which was mainly due to the influence of sintering shrinkage. The SVR measured by micro-CT was slightly higher than the theoretical one which is due to the increase of surface area caused by some surface micro-fractures in the sintered sample. The P-800 sample group possessed the highest SVR, which was directly correlated with the porosity. The linear shrinkage and the roughness average (Ra) of the four types of scaffolds showed no significant differences (Table 3). In addition, we also measured the surface roughness of the porous HA scaffolds. The results showed that the Ra value of the porous HA scaffolds was 25.4 ± 3.8 μm, which was much higher than that of the hardystonite scaffolds. The representative images of the scaffolds' surfaces over 300 × 200 μm areas were shown in Figure S2.

3.2. Evaluation of mechanical properties and in vitro bio-dissolution

A compressive measurement was carried out to evaluate the structural stability of the porous bioceramics *in vitro*. Among the four groups of scaffolds, the P500 and P800 samples exhibited the highest and the lowest compressive strength (46.3 ± 6.9 MPa, 6.9 ± 0.3 MPa), respectively. The P800-500 and P500-800 groups with different graded pore structures showed intermediate strengths (21.8 ± 3.9 MPa, 13.4 ± 1.9 MPa, respectively) (Fig. 3A). The representative stress-strain curves of the four groups followed a similar trend under compression load (Fig. 3B).

The macroporous bioceramics were immersed in Tris buffer to probe the mass decrease and ion release levels for the long duration stage. The P500 and P800 samples exhibited the highest and the lowest mass residual (98.9 ± 0.3%, 95.6 ± 0.3%), respectively, after immersion for 6 weeks, while the P800-500 and P500-800 samples with graded pore structures showed mild mass loss at the end of this immersion stage (Fig. 3C). Evidently, all of these macroporous biomaterials exhibited very poor dissolution characteristics during the long duration stage of *in vitro* immersion. This could be confirmed by the ion release dosage in the Tris buffer (Fig. 3D–F). The ion concentrations of Ca, Si and Zn increased within the first week, but the increase was slow and became gradually stable in the buffer medium during the next three weeks (from 7 to 28 days). However, it is worth noting that the changes in zinc ion

Table 3
Linear shrinkage and surface roughness of four groups of scaffolds.

Hardystonite scaffolds	X–Y Linear shrinkage (%)	Z Linear shrinkage (%)	Surface roughness
			Ra (μm)
P500	16.5 ± 0.3	17.3 ± 1.5	1.8 ± 0.3
P800-500	16.8 ± 0.1	17.0 ± 0.9	1.8 ± 0.2
P500-800	15.7 ± 0.7	17.8 ± 1.7	2.0 ± 0.4
P800	17.2 ± 0.9	17.9 ± 1.2	2.3 ± 0.5

Table 2
Structural characteristics of hardystonite scaffolds.

Hardystonite scaffolds	Unit size (mm)	Pore size (μm)		Porosity (%)		Surface to volume ratio (SVR, mm^{-1})	
		CAD	micro-CT	CAD	micro-CT	CAD	micro-CT
P500	1.5	500	462.4 ± 13.6	38.7	32.7 ± 1.9	5.6	6.4 ± 0.3
P800-500	1.5	800-650-500	563.9 ± 18.0	48.1	47.6 ± 3.0	6.4	7.7 ± 0.3
P500-800	1.5	500-650-800	570.4 ± 19.2	61.6	56.4 ± 1.2	8.4	9.9 ± 0.7
P800	1.5	800	784.2 ± 14.3	69.3	63.7 ± 1.3	9.3	11.0 ± 1.2

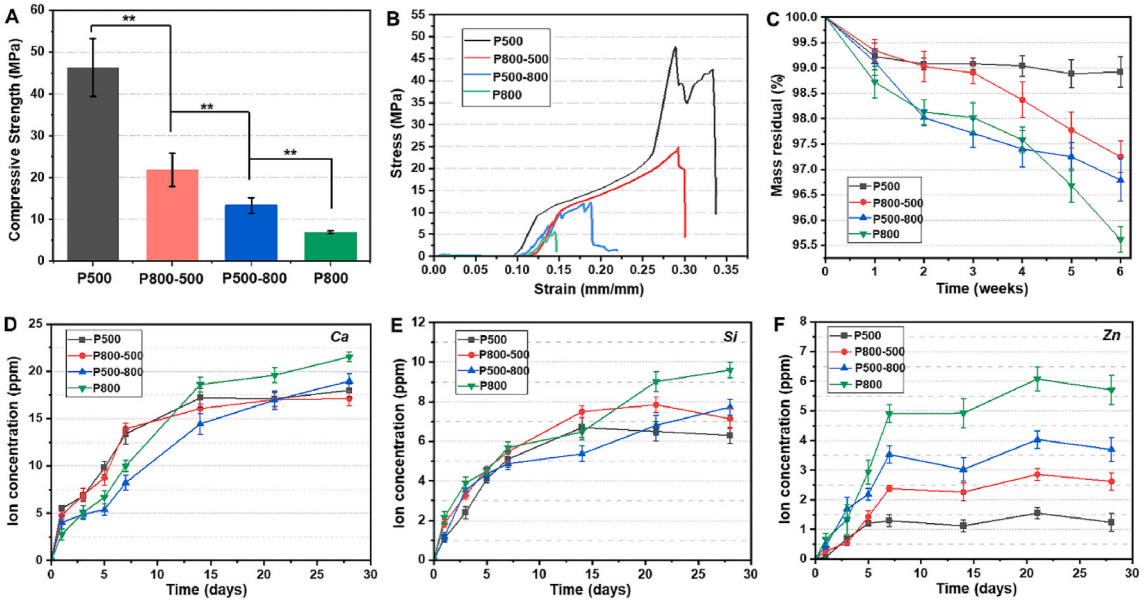

Fig. 3. (A) The compressive strength and (B) representative stress-strain curves of four groups of hardystonite scaffolds (**$p < 0.01$); (C) Mass residual of the scaffolds immersed in Tris buffer for 6 weeks; (D–F) Changes in Ca, Si, and Zn ion concentrations in Tris buffer during immersion process.

concentration displayed a correlation with the pore structures of the macroporous bioceramics (Fig. 3F). The P500 and P800 sample groups showed the highest and the lowest ionic concentration (~1.0–1.5 and ~5.0–6.0 ppm), respectively, and the two graded pore sample groups present intermediate ionic concentrations (~2.5–3.0 and ~3.0–4.0 ppm) after 7 days.

3.3. *In vitro evaluation of antibacterial potential*

The sintered hardystonite scaffolds and HA scaffolds were challenged with *S. aureus* and *E. coli* suspensions at a concentration of 5×10^7 CFU/mL. As shown in Fig. 4A, the density of viable bacterial clones on the substrates was obviously decreased as compared with that placed directly on the well (control). The quantitative analyses also confirmed that all groups of hardystonite scaffolds had excellent antibacterial properties (inhibitory rate ~70–90%) against both Gram-positive *S. aureus* and Gram-negative *E. coli* bacteria (Fig. 4B&C). In addition, the antibacterial properties of hardystonite scaffolds were significantly higher than those of HA scaffolds ($p < 0.01$). There was no significant difference in the inhibition rate against *S. aureus* among the

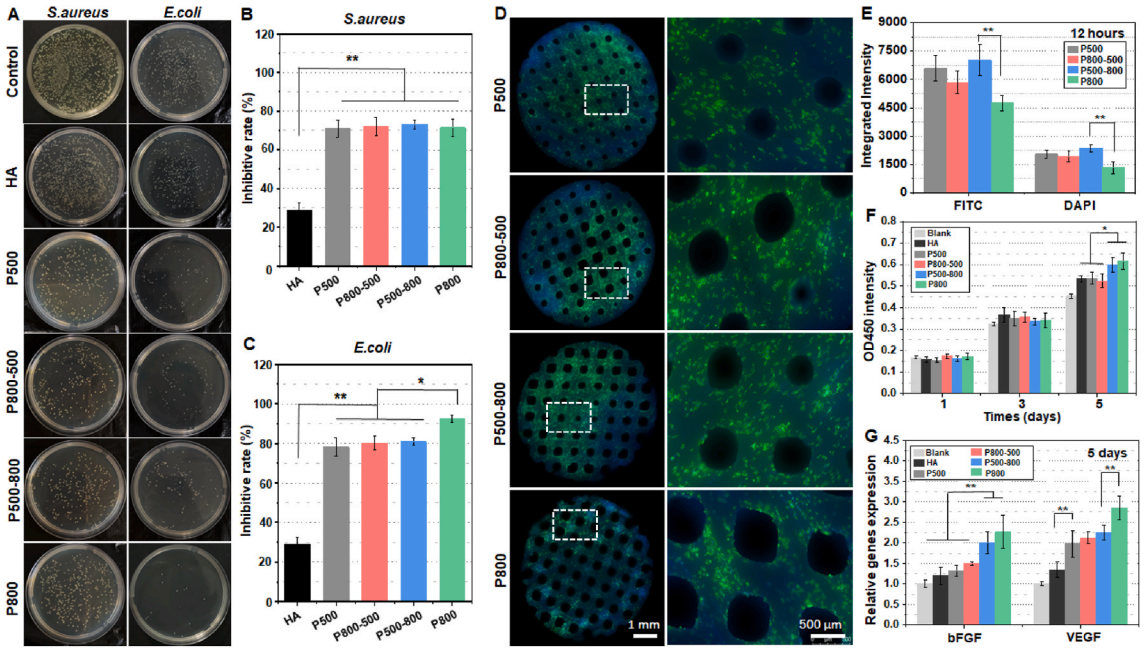

Fig. 4. (A) Colony-forming units of *S. aureus* and *E. coli* inoculated on HA scaffolds and four groups of hardystonite scaffolds for 12 h. Inhibitory rate of the scaffolds against (B) *S. aureus* and (C) *E. coli*. (D) Fluorescence microscopic images of HUVECs stained with F-actin (green) and DAPI (blue) after seeded on hardystonite scaffolds for 12 h. (E) The quantitative analysis of integrated fluorescence intensity of FITC and DAPI. (F) Viability of HUVECs seeded on HA scaffolds and four groups of hardystonite scaffolds for 1, 3 and 5 days. The cell culture plates without scaffolds were used as the blank control. (G) The angiogenesis genes bFGF and VEGF expression of HUVECs seeded on the test scaffolds for 5 days. (*$p < 0.05$, **$p < 0.01$).

four groups of hardystonite scaffolds, while the inhibition rate against *E. coli* in the P800 group was much higher in comparison with the other three groups ($p < 0.05$).

3.4. In vitro evaluation of cell viability on the bioceramics

Fig. 4D shows the fluorescence microscopic images of the distribution of HUVECs adhered to the hardystonite scaffolds with different macroporous structure. After 12 h of culture, the cells were more densely adhered onto the three groups of samples, except for the P800 group, in which the cells exhibited a relatively lower density. Moreover, the quantitative analysis involving the integrated fluorescence intensity of FITC and DAPI indicated that the cell density on the P500-800 samples was significantly higher than that on the P800 samples ($p < 0.01$; Fig. 4E).

The CCK-8 cell viability analysis (Fig. 4F) indicated that HUVECs seeded onto the four groups of hardystonite bioceramics kept a sustained proliferation activity throughout the observation period. Moreover, HUVECs seeded onto the P500-800 and the P800 scaffolds showed a significantly higher proliferation rate than those on tissue culture plastic (Blank), HA, P500 and P800-500 scaffolds on the 5th day. We also determined the expression of angiogenesis genes at day 5 of seeding the HUVECs on the test scaffolds. The quantitative analysis (Fig. 4G) indicated that the gene expression of bFGF was significantly increased in P500-800 and P800 groups, as compared with tissue culture plastic (Blank), HA, P500 and P800-500 groups. The P800 group exhibited the most efficient angiogenesis in the gene expression of VEGF. The four hardystonite groups were all superior to tissue culture plastic and HA groups in the gene expression of VEGF.

3.5. In vivo evaluation of vascularization in the macroporous bioceramics

In order to systematically evaluate the effect of pore structure on vascularization efficacy *in vivo*, an experimental animal model involving embedding the scaffolds beneath the dorsal muscle on the dorsum of rabbits was implemented. Fig. 5A&B show the scaffold embedding surgical procedure and the overall wound appearance after 6 weeks, respectively. Generally speaking, the back skin incision was completely healed, and no obvious inflammation or edema were seen around the implantation zone, implying the expected histocompatibility of the implants. According to the explanted specimens at different time stages (Fig. 5C), it could be confirmed that all of bioceramic scaffolds displayed good biocompatibility with the muscle tissue, and vascular traces were visible on the surface layer of the porous bioceramics.

Vascularization degree in the macroporous bioceramic was revealed by H&E staining and observation. The sections were divided into central part and peripheral part (4.5–9.0 mm from the center of the scaffolds) for evaluation. As shown in Fig. 6A, newly formed blood vessels could be seen in the peripheral pores in each group 2 weeks after implantation, and the blood vessels were all small in size. Four weeks after implantation, larger size blood vessels could be seen in the peripheral pores in the P500-800 and P800 groups, while samples in the other two groups were still dominated by smaller blood vessels (Fig. S3). After 6 weeks, bundles of muscle fibers were visible in the peripheral pores of the P500-800 and P800 groups, suggesting that muscle tissue had infiltrated into the porous bioceramics, and the blood vessels in the central pore regions of the P500-800 and P800 groups were more abundant.

In the histomorphometric analysis, the number and diameter of newly formed blood vessels at different times were determined, as shown in Fig. 6B. Interestingly, the number of blood vessels in the peripheral and centeral regions in the P500-800 and P800 groups was significantly higher than those in the P500 and P800-500 groups at 2 weeks ($p < 0.05$). After 4 weeks, no significant difference could be observed in the number of blood vessels in the periphery among the four groups, but the vessel diameters in the peripheral regions in the P500-800 and P800 groups were significantly larger than those in the other two groups. At 6 weeks, no significant difference could be found in the number of vessels in the peripheral and central regions, while the mean diameter of vessels in the central regions in the P500-800 and P800 groups was ~68 and ~89 μm, respectively, which were much higher than those in the P800-500 and P500 groups ($p < 0.01$).

3.6. In situ evaluation of orbital implant reconstruction

In this study, spherical hardystonite orbital implants of 12 mm diameter with two different graded porous structure were designed for an *in situ* animal model of enucleation (Fig. 7A&7B). The synthetic HA orbital implant (Ø 12 mm) was used as control. The outward appearance and micro-CT reconstructed cross-section images of three spherical samples were shown in Fig. 7C. The *in situ* rabbit enucleation model

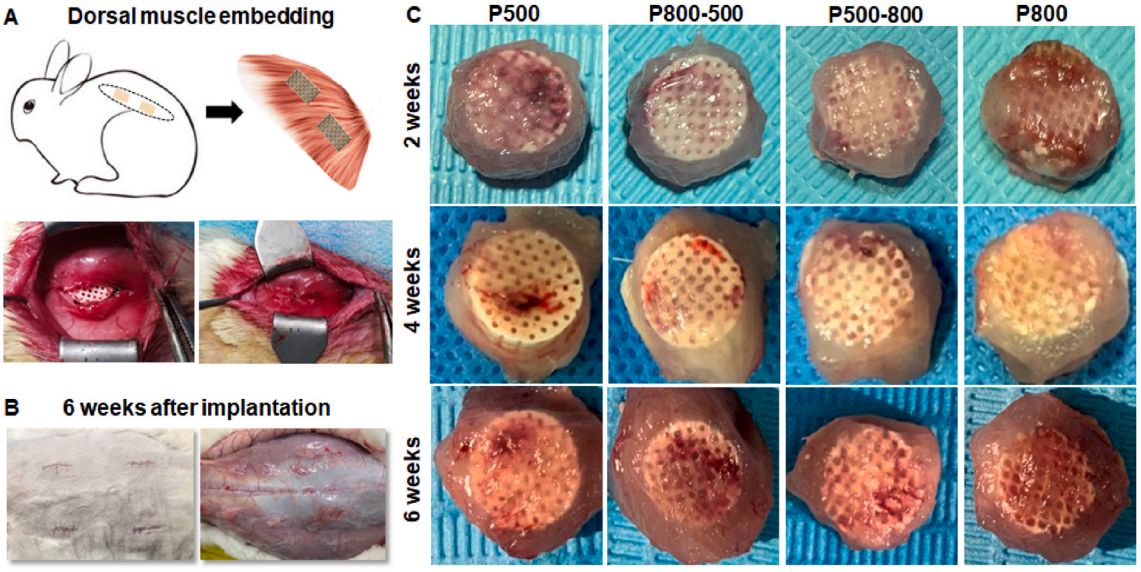

Fig. 5. (A) Schematic illustration of scaffolds embedding in dorsal muscle of New Zealand rabbits. (B) Overall wound appearance of the implantation zone after 6 weeks. The skin incision was completely healed, and no obvious inflammation or edema were seen around the implantation zone. (C) Outward appearance of harvest implants at 2, 4 and 6 weeks.

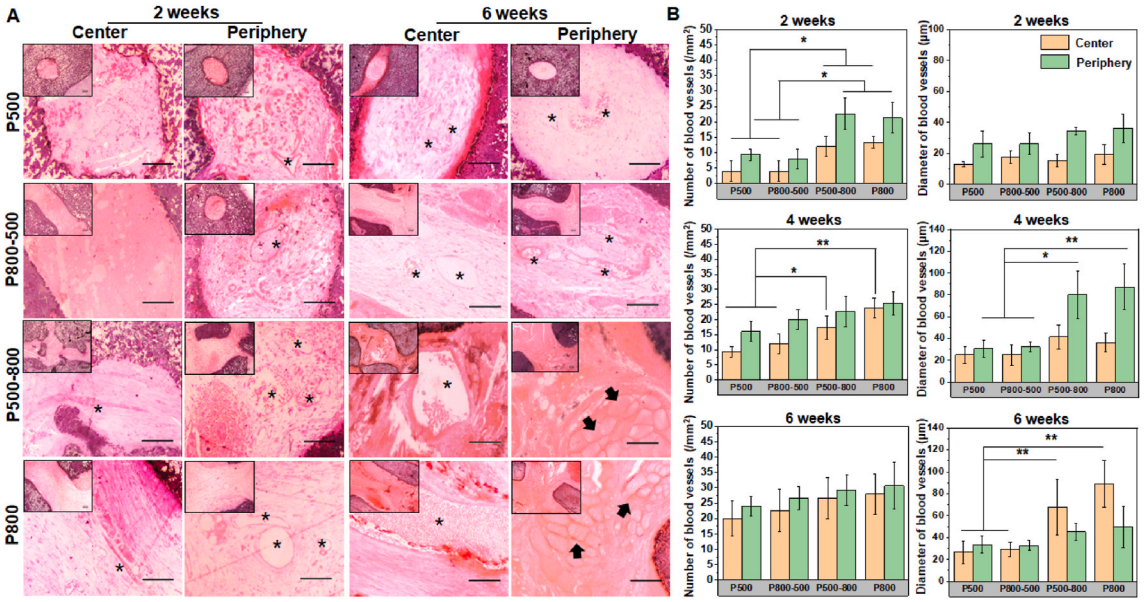

Fig. 6. (A) H&E staining of the scaffolds after embedding in dorsal muscle for 2 and 6 weeks. Inset images show the morphology at low magnification. The asterisks indicating newly formed blood vessels. The arrows showing muscle fiber tissue. Scale bar: 100 μm. (B) The number and mean size of newly formed blood vessels in scaffolds after embedding in dorsal muscle for 2, 4 and 6 weeks. (*$p < 0.05$, **$p < 0.01$).

process briefly consisted of removing the eyeball from the orbit and implanting the spherical sample to repair the orbital volume defect (seen in Fig. 7D). The operated eyes were continuously observed after surgery, and they showed no infection or implant exposure. Four weeks after implantation, the conjunctival sac of the operated eye was fully healed and stabilized in the sP800-500 and sP500-800 group, while the HA group still had a small amount of exudation and mild inflammatory reaction in the wound area (Fig. 7E). All the harvested spherical implants were well integrated into intra-orbital soft tissue (Fig. 7E).

According to the histological observation (Fig. 7F), the H&E staining images revealed that fibrovascular tissue had grown into the periphery pore region in the sP800-500 implant 4 weeks after implantation, but no obvious fibrovascular tissue was observed in the central pore region. As for the sP500-800 implant, fibrovascular tissue had fully grown into the central pore region 4 weeks after implantation. Meanwhile, typical vascular morphology could be observed in the periphery and central pore regions. Although a large number of small blood vessels infiltrating into the periphery pore region of the HA implant, there was still an area in the central region of the implant with no obvious fibrovascular tissue. Additionally, the quantitative analysis involving the fibrovascularization degree of scaffolds confirmed that the extent of fibrovascular ingrowth was about 63.9 ± 1.3% in the HA group, 48.5 ± 3.2% in the sP800-500 group, while it involved the entire scaffold in the sP500-800 group.

4. Discussion

For over a century, orbital implants have been applied following the surgical removal of the eyeball [36]. With the development of porous device designs, improved orbital implants have made a significant contribution to reduce complications and improve cosmesis. Unfortunately, some drawbacks of today's orbital implants still lead to the risk of implant migration and exposure, postoperative infections, and low motility. In the present study, we attempt to resolve the long-term problems in orbital reconstruction focusing on three key influencing factors, including material choice, pore architecture feature and manufacture technology. It is reasonable to consider that the new Ca–Zn-silicate bioceramic, i.e., hardystonite, is the promising candidate for developing multifunctional orbital implants because of its high biological stability, good biocompatibility, and significant antibacterial potential. On the other hand, the CAD-based DLP technique is an intriguing manufacturing approach to precisely control the pore architecture (including pore geometry, size, and interconnectivity) and enable finely tailored pore structures (e.g., curved pore surface, graded pore size, selected pore morphology). Accordingly, the spherical hardystonite porous implants with graded pore architectures were successfully fabricated in this study, and they demonstrated fast vascularization in the rabbit enucleation model.

In general, the orbital implant is regarded as a permanent device with a low level of biodegradation and highly stabilized structure to maintain socket volume for the patient's lifetime and withstand the mechanical pressure of the surgical insertion. Hardystonite bioceramic, incorporating Zn into the Ca–Si oxide system, has shown a more controlled biodegradation rate than calcium silicate and zinc silicate [13,34,37]. Zreiqat et al. reported that the mass decay of hardystonite scaffolds in SBF is less than 1% after immersion for 7 days [38]. Moreover, hardystonite bioceramic was shown to possess higher mechanical strength compared with pure hydroxyapatite and wollastonite bioceramic, and thus is more conductive to preparing stable porous scaffolds [34,39]. According to Andrea et al. hardystonite bioceramics could also be produced starting from preceramic polymers and suitable fillers in the form of 3D printed scaffolds by a single step firing treatment, which providing a combination of synthesis and shaping [39]. However, this approach did not yield mechanically strong porous scaffolds as expected. Therefore, the solid solutions or the additive-assisted sintering strategy was thought to be an alternative route to develop stronger porous scaffolds of hardystonite-based ceramics [40,41]. In our study, the hardystonite powders were synthesized by the sol-gel process, and the purity of the powders could be easily controlled by high calcination temperature (>1200 °C). Although the fabrication of 3D printed porous hardystonite scaffolds relied on the previously synthesized powders, the sintered porous samples exhibited comparatively high mechanical strength. On the other hand, our research has indicated that the mechanical strength and bio-dissolution of such macroporous bioceramics are strongly dependent on the parameters of porous structure (Fig. 3), and that the graded pore samples exhibit acceptable compressive strength (>10 MPa) and extremely low biodegradation rate (mass loss <3.5% in pure aqueous medium within 6 weeks). On the contrary, the

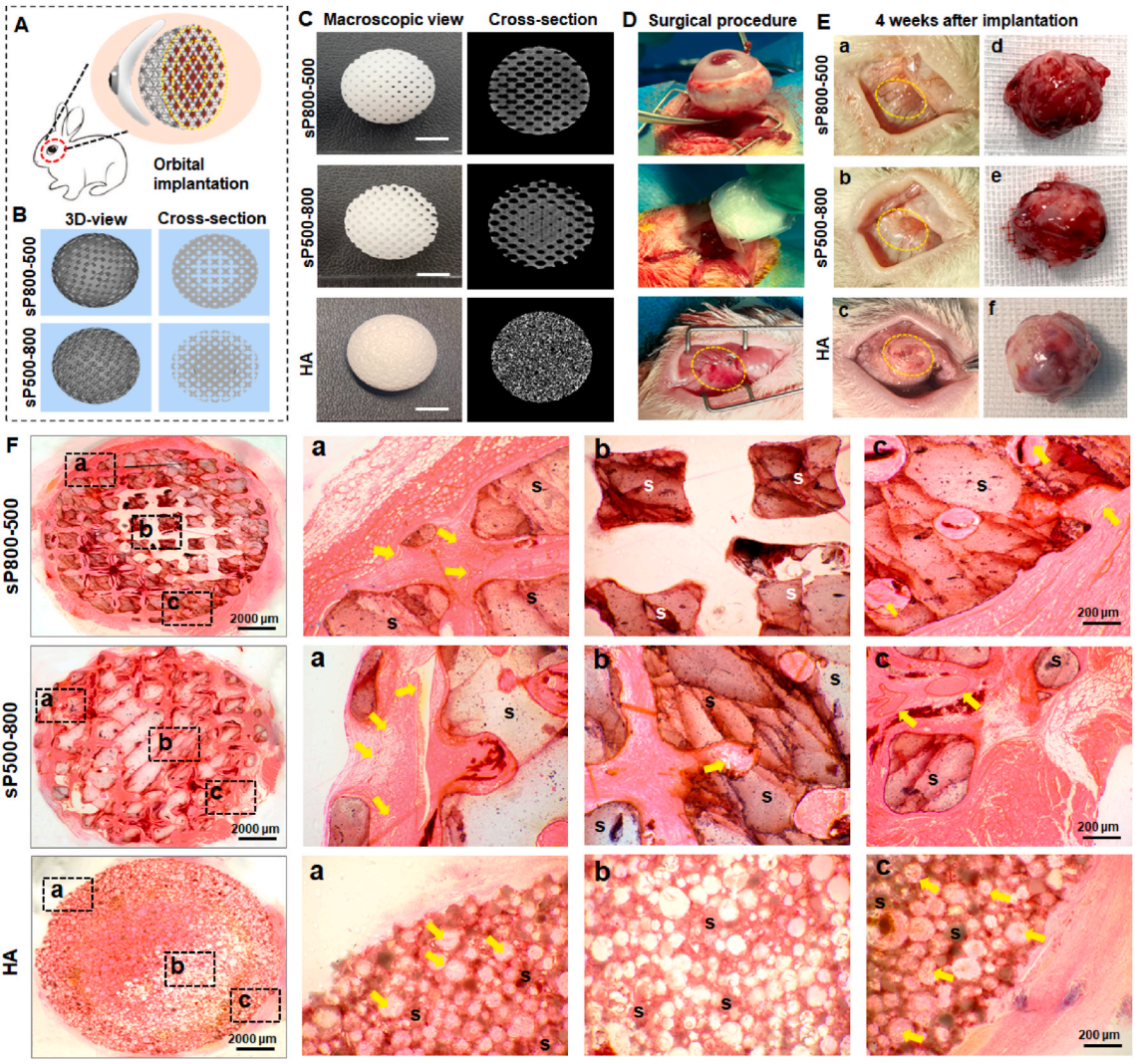

Fig. 7. (A) Schematic illustration of spherical scaffolds implanted in the rabbit anophthalmic sock after enucleation. (B) The CAD models of two different graded pore structure design of spherical scaffolds. (C) Outward appearance and micro-CT reconstructed cross-section images of two different graded porous hardystonite implants and HA implant. (D) The surgical procedure of enucleation and orbital implantation. (E) Postoperative appearance of conjunctival sac (a, b, c) and harvest scaffolds (d, e, f) 4 weeks after implantation. Yellow dotted circles mark conjunctival sac wounds. (F) H&E staining of harvest scaffolds. (a–c) show different regions of the scaffolds. S: scaffolds. Yellow arrows point out newly formed blood vessels.

mechanical strength of P800 scaffolds was significantly reduced and the biodegradation rate was comparatively higher. As a whole, the higher the porosity, the higher the degradation rate and the weaker the compressive resistance. As expected, the higher porosity and SVR are conducive to the more rapid ion exchange between biomaterial and aqueous buffer [42], which may accelerate the dissolution of ions from the surface layer of the pore wall. In this aspect, the Zn ion release behavior is directly correlated with the pore dimension and porosity of porous bioceramics. It is evident that the graded pore structure design can effectively regulate the pore size and physicochemical properties of macroporous bioceramics.

It is worth mentioning that infection derived from the colonization of biomaterials by microorganisms is one of the main complications associated with medical implants. However, the conventional approaches used in the clinic, including the pre-soaking treatment of orbital implants in antibiotics or the usage of intravenous or oral antibiotic therapies, are losing their market [43]. Therefore, the intrinsic antimicrobial properties of a biomaterial are increasingly expected to contribute to clinical success. In this study, Fig. 4 showed that all of the tested hardystonite bioceramics with different pore architectures exhibited significant antibacterial activity (inhibitory rate of 70–90%) against *S. aureus* and *E. coli* assessed in a very short time period (12 h). Zinc plays a determining role in the antibacterial effect of hardystonite bioceramic. Although the relevant mechanism is still unknown, some studies have suggested that Zn ions interact with microbe cell surfaces, changing membrane charge and causing breakdown of bacteria [44,45]. Moreover, a previous study found that the antibacterial efficacy of the Zn-modified coatings against *E. coli* was related to Zn content [16]. In our study, the high-porosity P800 scaffolds showed higher Zn ion dosage *in vitro* with time (Fig. 3), which may also contribute to enhancing the inhibitory rate against *E. coli*.

It is well agreed that the optimization of porous structures is important for effectively regulating cell response in tissue engineering. As for bone substitutes, small pores are beneficial for cell seeding, but they limit cell viability, cell proliferation and differentiation [46]. Our results indicated similar responses of HUVECs seeded on the macroporous hardystonite bioceramics. The P800 groups had the lowest cell adhesion, while they had the highest cell viability as well as the highest expression of angiogenesis-related genes (Fig. 4). On the one hand, high porosity and/or large pore size is accompanied by high cell permeability, which usually reduces the time of cell adhesion on the substrate [47]. On the other hand, porous biomaterials with larger pores feature

higher oxygen diffusion into the interior region, which may result in higher cell viability [48]. Notably, the graded pore bioceramics, especially those in the P500-800 group, showed a significant improvement in cell adhesion, and they also exhibited increased cell viability and angiogenesis-related gene expression (Fig. 4), which is consistent with the results in the literature [49]. Therefore, our novel graded pore bioceramics are more conducive to the effective interaction between angiogenic cells and biomaterial substitute.

Angiogenesis is the formation of small branches at the end of existing host blood vessels, which grow into the interior of the implant [50]. The pore architecture within a porous implant provides the space for tissue and blood vessels to grow, hence it plays an important role in vascularization. Previous studies have established that macropores over 400 μm could trigger larger-diameter blood vessels and less fibrous tissue ingrowth [51]. Larger pores are preferable for the delivery of oxygen and nutrients to cells inside substitutes and consequently for improving blood vessel formation. In this work, the vascularization ability of macroporous hardystonite bioceramics was evaluated in a rabbit' dorsal muscle embedding model *in vivo* (Figs. 5 and 6). Evidently, the pore size significantly affected the number of blood vessels in the early stage. However, during the late stage, the pore size had no significant effect on the number of blood vessels, while the blood vessel diameter was significantly increased with the pore size. As for the graded porous implants, the blood vessels diameter in the periphery of samples in the P500-800 group was remarkably larger than those in the center in the P800-500 group. It can be concluded that the peripheral small pores inhibit the ingrowth of large vessel into the central large pores, which is consistent with the result of previous studies [25]. Moreover, the interconnection of pore windows, acting as the bottleneck for vascular invasion, is another key factor of scaffolds vascularization [52,53]. Small pore windows would preferentially permit small blood vessels' invasion, and such pore architecture may inevitably limit the penetration of blood vessels into the central region of scaffolds, irrespective of the pore size in their central region. Accordingly, graded radial pore structure with pore size gradually increasing from center to periphery yield better vascularization capability.

Fast vascularization in orbital implants, which may improve the implant integration with the host soft tissue and reduce the risk of complications, is one of critical factors for successful clinical outcomes. As fibrovascular tissue grows into the macropores of the porous implant, orbital soft tissue can be mechanically fixed to the implant, thereby reducing implant migration and exposure [3]. At the same time, abundant blood vessels provide immune support, which is conducive to wound healing and reduces the risk of postoperative infections [7]. According to long-term clinical results, coralline hydroxyaptite implants with 80% in porosity achieved a very fast vascularization rate, followed by synthetic hydroxyapatite implants (50–65% in porosity), and finally Medpor (~41% in porosity) [54,55]. Despite the better vascularization performance of the P800 group in the dorsal muscle embedding experiment, the structural stability and mechanical properties of this architecture are unable to withstand the extrusion pressure during orbital implantation. Hence, the graded pore implants with opposite pore size distribution were preferentially used in the rabbit enucleation model. Four weeks after implantation, the extent of fibro-vascularization was about 48.5 ± 3.2% in the sP800-500 group and 100% in the sP500-800 group via histologic evaluation (Fig. 7). In addition, the extent of fibro-vascularization in the HA group in this study was about 63.9 ± 1.3%, which was higher than that in the sP800-500 group. However, delayed healing of conjunctival wounds possibly caused by the rough surface of HA implant was observed. The previous literatures reported that the extent of fibrovascularization in 12-mm porous polyethylene implants was about 26% [35], while the coralline hydroxyapatite implants were completely vascularized in a rabbit model at 3–4 weeks [56]. Thus, the vascularization rate of sP500-800 hardystonite implant was shown to be comparable to that of the fastest coralline hydroxyapatite.

Overall, computer-assisted topology and graded pore design could tailor and even optimize the performance of hardystonite implants. Addictive manufacturing has a great advantage in fabricating porous substitutes with precisely controlled microstructure [57]. Moreover, this technique can easily adjust the morphology and size of porous implants to fabricate custom-made devices, mimicking the aesthetic features of the contralateral eye. Although our studies have provided a novel insight into the structural design and material selection of orbital implants, more samples for long-term *in vivo* evaluation and systematic comparisons with clinical materials are needed. Also, we need to further study the permeability and fluid flow characteristics of graded pore implants, which would be helpful to understand the interaction mechanism between cells, tissues and material pore architecture, and to finally optimize the structural design of next-generation orbital implants.

5. Conclusions

In summary, we have successfully developed a novel graded porous hardystonite scaffolds for orbital reconstruction through a computer-assisted topology design and DLP technology. The characteristics of hardystonite bioceramics with four types of pore architecture and precisely controlled IWP curved-surface pore geometry were systematically evaluated. The results showed that the graded porous implants exhibit sparing biodegradation, appropriate mechanical strength and excellent antibacterial potential. In particular, the P500-800 implants could significantly improve cell seeding ability, and they also yielded high cell viability and angiogenesis-related gene expression. A rabbit model of ectopic implantation in dorsal muscle showed that the P500-800 implants were more favorable for large and abundant new blood vessel infiltration. In addition, the spherical implants exhibited fast vascularization and excellent post-operative recovery effect in a rabbit enucleation model. These findings suggest that the finely controlled graded porous hardystonite implants with radial pore architectures from center to periphery are especially favorable for future orbital implantation in the clinic.

CRediT authorship contribution statement

Jingyi Wang: Conceptualization, Methodology, Software, Investigation, Formal analysis, Data curation, Writing – original draft. **Yiyu Peng:** Methodology, Investigation, Validation. **Menglu Chen:** Investigation, Data curation. **Xizhe Dai:** Investigation, Data curation. **Lixia Lou:** Formal analysis, Resources. **Changjun Wang:** Methodology, Resources. **Zhaonan Bao:** Software. **Xianyan Yang:** Methodology, Resources. **Zhongru Gou:** Conceptualization, Methodology, Supervision, Writing – review & editing. **Juan Ye:** Conceptualization, Supervision, Writing – review & editing, Funding acquisition.

Declaration of competing interest

The authors declare that they have no known competing financial interests or personal relationships that could have appeared to influence the work reported in this paper.

Acknowledgements

Authors would like to acknowledge financial support from the National Natural Science Foundation of China (81870635, 82000948). the National Key Research and Development Program of China (2017YFE0117700) and Natural Science Foundation of Zhejiang Province (LY20H120007).

Appendix A. Supplementary data

Supplementary data to this article can be found online at https://doi.org/10.1016/j.bioactmat.2021.12.028.

References

[1] O.H. Ababneh, E.A. AboTaleb, M.A. Abu Ameerh, Y.A. Yousef, Enucleation and evisceration at a tertiary care hospital in a developing country, BMC Ophthalmol. 15 (2015), 120, https://doi.org/10.1186/s12886-015-0108-x.

[2] P. Viswanathan, M.S. Sagoo, J.M. Olver, UK national survey of enucleation, evisceration and orbital implant trends, Br. J. Ophthalmol. 91 (2007) 616–619, https://doi.org/10.1136/bjo.2006.103937.

[3] R. Chalasani, L. Poole-Warren, R.M. Conway, B. Ben-Nissan, Porous orbital implants in enucleation: a systematic review, Surv. Ophthalmol. 52 (2007) 145–155, https://doi.org/10.1016/j.survophthal.2006.12.007.

[4] J.S. Yoon, H. Lew, S.J. Kim, S.Y. Lee, Exposure rate of hydroxyapatite orbital implants, Ophthalmology 115 (2008) 566–572, https://doi.org/10.1016/j.ophtha.2007.06.014.

[5] J. Ye, Q. Gao, J.J. He, T. Gao, Q.Y. Ning, J.J. Xie, Exposure rate of unwrapped hydroxyapatite orbital implants in enucleation surgery, Br. J. Ophthalmol. 100 (2016) 860–865, https://doi.org/10.1136/bjophthalmol-2015-307412.

[6] S.K. Jung, W.K. Cho, J.S. Paik, S.W. Yang, Long-term surgical outcomes of porous polyethylene orbital implants: a review of 314 cases, Br. J. Ophthalmol. 96 (2012) 494–498, https://doi.org/10.1136/bjophthalmol-2011-300132.

[7] F. Baino, I. Potestio, Orbital implants: state-of-the-art review with emphasis on biomaterials and recent advances, Mater. Sci. Eng. C-Mater. Biol. Appl. 69 (2016) 1410–1428, https://doi.org/10.1016/j.msec.2016.08.003.

[8] E.V. Francesco Baino, Elisa Fiume, Oscar Peitl, Edgar D. Zanotto, Simone M. Brandão, Silvana A. Schellini, Bioactive glass and glass-ceramic orbital implants, Int. J. Appl. Ceram. Technol. 16 (2019) 1850–1863, https://doi.org/10.1111/ijac.13236.

[9] F. Baino, G.G. di Confiengo, M.G. Faga, Fabrication and morphological characterization of glass-ceramic orbital implants, Int. J. Appl. Ceram. Technol. 15 (2018) 884–891, https://doi.org/10.1111/ijac.12837.

[10] J.J. Li, C.R. Dunstan, A. Entezari, Q. Li, R. Steck, S. Saifzadeh, A. Sadeghpour, J. R. Field, A. Akey, M. Vielreicher, O. Friedrich, S.I. Roohani-Esfahani, H. Zreiqat, A novel bone substitute with high bioactivity, strength, and porosity for repairing large and load-bearing bone defects, Adv. Healthc. Mater. 8 (2019), 1801298, https://doi.org/10.1002/adhm.201801298.

[11] Y.J. No, X. Xin, Y. Ramaswamy, Y. Li, S. Roohaniesfahani, S. Mustaffa, J. Shi, X. Jiang, H. Zreiqat, Novel injectable strontium-hardystonite phosphate cement for cancellous bone filling applications, Mater. Sci. Eng. C-Mater. Biol. Appl. 97 (2019) 103–115, https://doi.org/10.1016/j.msec.2018.11.069.

[12] W. Zhang, G. Wang, Y. Liu, X. Zhao, D. Zou, C. Zhu, Y. Jin, Q. Huang, J. Sun, X. Liu, X. Jiang, H. Zreiqat, The synergistic effect of hierarchical micro/nano-topography and bioactive ions for enhanced osseointegration, Biomaterials 34 (2013) 3184–3195, https://doi.org/10.1016/j.biomaterials.2013.01.008.

[13] C. Wu, Y. Ramaswamy, J. Chang, J. Woods, Y. Chen, H. Zreiqat, The effect of Zn contents on phase composition, chemical stability and cellular bioactivity in Zn-Ca-Si system ceramics, J. Biomed. Mater. Res. Part B 87 (2008) 346–353, https://doi.org/10.1002/jbm.b.31109.

[14] H. Lu, N. Kawazoe, T. Tateishi, G. Chen, X. Jin, J. Chang, In vitro proliferation and osteogenic differentiation of human bone marrow-derived mesenchymal stem cells cultured with hardystonite ($Ca_2ZnSi_2O_7$) and β-TCP ceramics, J. Biomater. Appl. 25 (2010) 39–56, https://doi.org/10.1177/0885328209342469.

[15] K. Li, J. Yu, Y. Xie, L. Huang, X. Ye, X. Zheng, Chemical stability and antimicrobial activity of plasma sprayed bioactive $Ca_2ZnSi_2O_7$ coating, Journal of materials science. J. Mater. Sci.-Mater. Med. 22 (2011) 2781–2789, https://doi.org/10.1007/s10856-011-4454-9.

[16] K. Li, J. Yu, Y. Xie, L. Huang, X. Ye, X. Zheng, Effects of Zn content on crystal structure, cytocompatibility, antibacterial activity, and chemical stability in Zn-modified calcium silicate coatings, J. Therm. Spray Technol. 22 (2013) 965–973, https://doi.org/10.1007/s11666-013-9938-3.

[17] Z. Zhang, W. Li, Y. Liu, Z. Yang, L. Ma, H. Zhuang, E. Wang, C. Wu, Z. Huan, F. Guo, J. Chang, Design of a biofluid-absorbing bioactive sandwich-structured Zn-Si bioceramic composite wound dressing for hair follicle regeneration and skin burn wound healing, Bioact. Mater. 6 (2021) 1910–1920, https://doi.org/10.1016/j.bioactmat.2020.12.006.

[18] Y. Li, Y. Han, X. Wang, J. Peng, Y. Xu, J. Chang, Multifunctional hydrogels prepared by dual ion cross-linking for chronic wound healing, ACS Appl. Mater. Interfaces 9 (2017) 16054–16062, https://doi.org/10.1021/acsami.7b04801.

[19] H. Elsayed, A. Zocca, G. Franchin, E. Bernardo, P. Colombo, Hardystonite bioceramics from preceramic polymers, J. Eur. Ceram. Soc. 36 (2016) 829–835, https://doi.org/10.1016/j.jeurceramsoc.2015.10.034.

[20] S. Bose, S. Vahabzadeh, A. Bandyopadhyay, Bone tissue engineering using 3D printing, Mater. Today 16 (2013) 496–504, https://doi.org/10.1016/j.mattod.2013.11.017.

[21] I.R. Ali Entezari, Guanglong Li, Colin R. Dunstan, Pierre Rognon, Qing Li, Xinquan Jiang, Hala Zreiqat, Architectural design of 3D printed scaffolds controls the volume and functionality of newly formed bone, Adv. Healthc. Mater. 8 (2019), 1801353, https://doi.org/10.1002/adhm.201801353.

[22] J. Diao, H. Ding, M. Huang, X. Fu, F. Zou, T. Li, N. Zhao, C. Mao, Y. Wang, Bone defect model dependent optimal pore sizes of 3D-plotted beta-tricalcium phosphate scaffolds for bone regeneration, Small Methods 3 (2019), 1900237, https://doi.org/10.1002/smtd.201900237.

[23] A. Magnaudeix, J. Usseglio, M. Lasgorceix, F. Lalloue, C. Damia, J. Brie, P. Pascaud-Mathieu, E. Champion, Quantitative analysis of vascular colonisation and angio-conduction in porous silicon-substituted hydroxyapatite with various pore shapes in a chick chorioallantoic membrane (CAM) model, Acta Biomater. 38 (2016) 179–189, https://doi.org/10.1016/j.actbio.2016.04.039.

[24] V. Karageorgiou, D. Kaplan, Porosity of 3D biomaterial scaffolds and osteogenesis, Biomaterials 26 (2005) 5474–5491, https://doi.org/10.1016/j.biomaterials.2005.02.002.

[25] J. Li, T. Xu, W. Hou, F. Liu, W. Qing, L. Huang, G. Ma, Y. Mu, J. Weng, The response of host blood vessels to graded distribution of macro-pores size in the process of ectopic osteogenesis, Mater. Sci. Eng. C-Mater. Biol. Appl. 109 (2020), 110641, https://doi.org/10.1016/j.msec.2020.110641.

[26] S.H. Oh, I.K. Park, J.M. Kim, J.H. Lee, In vitro and in vivo characteristics of PCL scaffolds with pore size gradient fabricated by a centrifugation method, Biomaterials 28 (2007) 1664–1671, https://doi.org/10.1016/j.biomaterials.2006.11.024.

[27] A. Macchetta, I.G. Turner, C.R. Bowen, Fabrication of HA/TCP scaffolds with a graded and porous structure using a camphene-based freeze-casting method, Acta Biomater. 5 (2009) 1319–1327, https://doi.org/10.1016/j.actbio.2008.11.009.

[28] Y. Chen, D. Kent, M. Bermingham, A. Dehghan-Manshadi, G. Wang, C. Wen, M. Dargusch, Manufacturing of graded titanium scaffolds using a novel space holder technique, Bioact. Mater. 2 (2017) 248–252, https://doi.org/10.1016/j.bioactmat.2017.07.001.

[29] X. Wang, S. Xu, S. Zhou, W. Xu, M. Leary, P. Choong, M. Qian, M. Brandt, Y.M. Xie, Topological design and additive manufacturing of porous metals for bone scaffolds and orthopaedic implants: a review, Biomaterials 83 (2016) 127–141, https://doi.org/10.1016/j.biomaterials.2016.01.012.

[30] R.S. Ambekar, B. Kushwaha, P. Sharma, F. Bosia, M. Fraldi, N.M. Pugno, C. S. Tiwary, Topologically engineered 3D printed architectures with superior mechanical strength, Mater. Today 48 (2021) 72–94, https://doi.org/10.1016/j.mattod.2021.03.014.

[31] C. Han, Y. Li, Q. Wang, S. Wen, Q. Wei, C. Yan, L. Hao, J. Liu, Y. Shi, Continuous functionally graded porous titanium scaffolds manufactured by selective laser melting for bone implants, J. Mech. Behav. Biomed. Mater. 80 (2018) 119–127, https://doi.org/10.1016/j.jmbbm.2018.01.013.

[32] X.Y. Zhang, G. Fang, S. Leeflang, A.A. Zadpoor, J. Zhou, Topological design, permeability and mechanical behavior of additively manufactured functionally graded porous metallic biomaterials, Acta Biomater. 84 (2019) 437–452, https://doi.org/10.1016/j.actbio.2018.12.013.

[33] F. Lu, R. Wu, M. Shen, L. Xie, M. Liu, Y. Li, S. Xu, L. Wan, X. Yang, C. Gao, Z. Gou, Rational design of bioceramic scaffolds with tuning pore geometry by stereolithography: microstructure evaluation and mechanical evolution, J. Eur. Ceram. Soc. 41 (2021) 1672–1682, https://doi.org/10.1016/j.jeurceramsoc.2020.10.002.

[34] C.T. Wu, J. Chang, W.Y. Zhai, A novel hardystonite bioceramic: preparation and characteristics, Ceram. Int. 31 (2005) 27–31, https://doi.org/10.1016/j.ceramint.2004.02.008.

[35] D.R. Jordan, S. Brownstein, M. Dorey, V.H. Yuen, S. Gilberg, Fibrovascularization of porous polyethylene (Medpor) orbital implant in a rabbit model, Ophthalmic Plast. Reconstr. Surg. 20 (2004) 136–143, https://doi.org/10.1097/01.IOP.0000117341.28846.7F.

[36] P.H. Mules, Evisceration of the globe with artificial vitreous. 1884–1895, Adv. Ophthalmic Plast. Reconstr. Surg. 8 (1990) 69–72.

[37] C. Wu, Methods of improving mechanical and biomedical properties of Ca-Si-based ceramics and scaffolds, Expet Rev. Med. Dev. 6 (2009) 237–241, https://doi.org/10.1586/erd.09.3.

[38] H. Zreiqat, Y. Ramaswamy, C. Wu, A. Paschalidis, Z. Lu, B. James, O. Birke, M. McDonald, D. Little, C.R. Dunstan, The incorporation of strontium and zinc into a calcium-silicon ceramic for bone tissue engineering, Biomaterials 31 (2010) 3175–3184, https://doi.org/10.1016/j.biomaterials.2010.01.024.

[39] A. Zocca, G. Franchin, H. Elsayed, E. Gioffredi, E. Bernardo, P. Colombo, A. Bandyopadhyay, Direct ink writing of a preceramic polymer and fillers to produce hardystonite ($Ca_2ZnSi_2O_7$) bioceramic scaffolds, J. Am. Ceram. Soc. 99 (2016) 1960–1967, https://doi.org/10.1111/jace.14213.

[40] H. Elsayed, A.R. Romero, M. Picicco, J. Kraxner, D. Galusek, P. Colombo, E. Bernardo, Glass-ceramic foams and reticulated scaffolds by sinter-crystallization of a hardystonite glass, J. Non-Cryst. Solids 528 (2020), 119744, https://doi.org/10.1016/j.jnoncrysol.2019.119744.

[41] H. Elsayed, C. Gardin, L. Ferroni, B. Zavan, P. Colombo, E. Bernardo, Highly porous Sr/Mg-doped hardystonite bioceramics from preceramic polymers and reactive fillers: direct foaming and direct ink writing, Adv. Eng. Mater. 21 (2018), 1800900, https://doi.org/10.1002/adem.201800900.

[42] Y. Zhou, C. Wu, J. Chang, Bioceramics to regulate stem cells and their microenvironment for tissue regeneration, Mater, Today Off. 24 (2019) 41–56, https://doi.org/10.1016/j.mattod.2018.07.016.

[43] R. Anaya-Alaminos, N. Ibanez-Flores, I. Aznar-Pena, M. Gonzalez-Andrades, Antimicrobial biomaterials and their potential application in ophthalmology, J. Appl. Biomater. Funct. Mater. 13 (2015) 346–350, https://doi.org/10.5301/jabfm.5000253.

[44] Y.W. Wang, A. Cao, Y. Jiang, X. Zhang, J.H. Liu, Y. Liu, H. Wang, Superior antibacterial activity of zinc oxide/graphene oxide composites originating from high zinc concentration localized around bacteria, ACS Appl. Mater. Interfaces 6 (2014) 2791–2798, https://doi.org/10.1021/am4053317.

[45] Y. Su, I. Cockerill, Y. Wang, Y.X. Qin, L. Chang, Y. Zheng, D. Zhu, Zinc-based biomaterials for regeneration and therapy, Trends Biotechnol. 37 (2019) 428–441, https://doi.org/10.1016/j.tibtech.2018.10.009.

[46] F.S.L. Bobbert, A.A. Zadpoor, Effects of bone substitute architecture and surface properties on cell response, angiogenesis, and structure of new bone, J. Mat. Chem. B 5 (2017) 6175–6192, https://doi.org/10.1039/c7tb00741h.

[47] S. Van Bael, Y.C. Chai, S. Truscello, M. Moesen, G. Kerckhofs, H. Van Oosterwyck, J.P. Kruth, J. Schrooten, The effect of pore geometry on the in vitro biological

behavior of human periosteum-derived cells seeded on selective laser-melted Ti_6Al_4V bone scaffolds, Acta Biomater. 8 (2012) 2824–2834, https://doi.org/10.1016/j.actbio.2012.04.001.

[48] K. Kim, D. Dean, J. Wallace, R. Breithaupt, A.G. Mikos, J.P. Fisher, The influence of stereolithographic scaffold architecture and composition on osteogenic signal expression with rat bone marrow stromal cells, Biomaterials 32 (2011) 3750–3763, https://doi.org/10.1016/j.biomaterials.2011.01.016.

[49] A. Marrella, T.Y. Lee, D.H. Lee, S. Karuthedom, D. Syla, A. Chawla, A. Khademhosseini, H.L. Jang, Engineering vascularized and innervated bone biomaterials for improved skeletal tissue regeneration, Mater, Today Off. 21 (2018) 362–376, https://doi.org/10.1016/j.mattod.2017.10.005.

[50] R.A. Carano, E.H. Filvaroff, Angiogenesis and bone repair, drug discov, Today Off. 8 (2003) 980–989, https://doi.org/10.1016/s1359-6446(03)02866-6.

[51] B. Feng, Z. Jinkang, W. Zhen, L. Jianxi, C. Jiang, L. Jian, M. Guolin, D. Xin, The effect of pore size on tissue ingrowth and neovascularization in porous bioceramics of controlled architecture in vivo, Biomed. Mater. 6 (2011), 015007, https://doi.org/10.1088/1748-6041/6/1/015007.

[52] F. Bai, Z. Wang, J. Lu, J. Liu, G. Chen, R. Lv, J. Wang, K. Lin, J. Zhang, X. Huang, The correlation between the internal structure and vascularization of controllable porous bioceramic materials in vivo: a quantitative study, Tissue Eng. 16 (2010) 3791–3803, https://doi.org/10.1089/ten.TEA.2010.0148.

[53] M. Mastrogiacomo, S. Scaglione, R. Martinetti, L. Dolcini, F. Beltrame, R. Cancedda, R. Quarto, Role of scaffold internal structure on in vivo bone formation in macroporous calcium phosphate bioceramics, Biomaterials 27 (2006) 3230–3237, https://doi.org/10.1016/j.biomaterials.2006.01.031.

[54] P.A. Rubin, J.K. Popham, J.R. Bilyk, J.W. Shore, Comparison of fibrovascular ingrowth into hydroxyapatite and porous polyethylene orbital implants, Ophthalmic Plast. Reconstr. Surg. 10 (1994) 96–103, https://doi.org/10.1097/00002341-199406000-00005.

[55] T. Celik, D. Yuksel, M. Kosker, R. Kasim, S. Simsek, Vascularization of coralline versus synthetic hydroxyapatite orbital implants assessed by gadolinium enhanced magnetic resonance imaging, Curr. Eye Res. 40 (2015) 346–353, https://doi.org/10.3109/02713683.2014.922192.

[56] G.S. Gayre, W. Lipham, J.J. Dutton, A comparison of rates of fibrovascular ingrowth in wrapped versus unwrapped hydroxyapatite spheres in a rabbit model, Ophthalmic Plast. Reconstr. Surg. 18 (2002) 275–280, https://doi.org/10.1097/00002341-200207000-00008.

[57] S.A.M. Tofail, E.P. Koumoulos, A. Bandyopadhyay, S. Bose, L. O'Donoghue, C. Charitidis, Additive manufacturing: scientific and technological challenges, market uptake and opportunities, Mater. Today 21 (2018) 22–37, https://doi.org/10.1016/j.mattod.2017.07.001.